# Simulated wind farm wake sensitivity to configuration choices in the Weather Research and Forecasting model version 3.8.1

**Jessica M. Tomaszewski**[1] **and Julie K. Lundquist**[1,2]

[1]Department of Atmospheric and Oceanic Sciences, University of Colorado, 311 UCB, Boulder, CO 80309, USA

[2]National Renewable Energy Laboratory, Golden, CO, USA

**Correspondence:** Jessica M. Tomaszewski (jessica.tomaszewski@colorado.edu)

**Abstract.** Wakes from wind farms can extend over 50 km downwind in stably stratified conditions. These wakes can undermine power production at downwind turbines, adversely undermining revenue. As such, wind farm wake impacts must be considered in wind resource assessments, especially in regions of dense wind farm development. The open-source Weather Research and Forecasting (WRF) numerical weather prediction model includes a wind farm parameterization to estimate wind farm wake 10 effects, but model configuration choices can influence the resulting predictions of wind farm wakes. These choices include vertical resolution, horizontal resolution, and whether or not to include the addition of turbulent kinetic energy generated by the spinning wind turbines. Despite the sensitivity to model configuration, no clear guidance currently exists for these options. Here we compare simulated wind farm wakes produced by varying model configurations with observations from in situ meteorological observations near an onshore wind farm in flat terrain over several diurnal cycles. A WRF configuration 15 comprised of horizontal resolutions of 3 km or 1 km paired with a vertical resolution of 10 m provides the most accurate representation of wind farm wake effects, such as the correct surface warming and elevated wind speed deficit. The inclusion of turbine-generated turbulence is also critical to produce accurate surface warming and should not be omitted.

# 1 Introduction

Wind energy is growing rapidly to meet increasing energy demands while reducing carbon dioxide emissions. A wind turbine generates electricity by using momentum from the wind to turn its blades and generator, causing a downwind wake characterized by a reduction in wind speed and an increase in turbulence (Lissaman, 1979). The aggregate impact of these individual
10 turbine wakes can extend over 50 km downwind of a wind farm, particularly during stable conditions when little atmospheric convection is present to erode the wake (Christiansen and Hasager, 2005; Platis et al., 2018). Consequences of these wake effects include local changes to surface fluxes that can raise surface temperatures at night due to turbine-induced mixing of the nocturnal inversion (Baidya Roy, 2004; Baidya Roy and Traiteur, 2010; Zhou et al., 2012; Rajewski et al., 2013; Smith et al., 2013; Rajewski et al., 2016; Siedersleben et al., 2018a) and loss of power and revenue for downwind wind farms operating in
15 the wind speed deficit (Nygaard, 2014; Nygaard and Hansen, 2016; Nygaard and Newcombe, 2018; Lundquist et al., 2018). As wind farms continue dense development, wind farm wake impacts must be considered in wind resource assessments.

Several numerical simulation tools exist to assess wind farm wake effects. Large-eddy simulations (LES) provide fine-scale information of near-turbine meteorological impacts of wind turbines (Sørensen and Shen, 2002; Vermeer et al., 2003; Calaf et al., 2010; Troldborg et al., 2010; Sanderse et al., 2011; Churchfield et al., 2012; Archer et al., 2013; Aitken et al., 2014;
20 Mirocha et al., 2014; Abkar and Porté-Agel, 2015a, b; Vanderwende et al., 2016; Marjanovic et al., 2017; Tomaszewski et al., 2018). Simulating the turbine rotor and downstream flow with LES is useful, albeit computationally expensive, making realistic LES simulations of entire wind farms that can span 100s of km$^2$ unreasonable.

One approach to parameterizing turbines numerically in simulations with grid spacings of kilometers or more is to exaggerate surface roughness to represent the local reduction of wind speed of wind farm wakes (Keith et al., 2004; Frandsen et al., 2009;
25 Barrie and Kirk-Davidoff, 2010; Fitch, 2015). This enhanced surface roughness approach was later shown to produce erroneous predictions, including the wrong sign of surface temperature change through the diurnal cycle (Fitch et al., 2013a). Emeis and Frandsen (1993) proposed and later refined (Emeis, 2009) an analytical wind park model that considers both momentum loss and downward momentum flux, which accounts for the spatially averaged and stability dependent momentum-extraction coefficient by turbines. While the Emeis model incorporates the influence of additional wake characteristics, it lacks consideration
30 for turbine-scale interactions between the rotor layer and the surface (Fitch et al., 2012; Abkar and Porté-Agel, 2015a).

Alternatively, the turbine power and thrust curves can define the elevated momentum sink and turbulence generation of a wind turbine. The turbine power and thrust curves give the relationship between hub-height inflow wind speed, power produc-

tion, and force exerted onto the ambient air by a specific wind turbine type. The use of these turbine specifications can predict meteorological impacts of wind turbines at hub-height extending down to the surface, forming the basis for multiple wind farm parameterizations in mesoscale numerical weather prediction models such as the Wind Farm Parameterization (WFP) (Fitch et al., 2012; Fitch, 2016), the Explicit Wake Parametrisation (Volker et al., 2015), the Abkar and Porté-Agel (2015b) Parameterization, and a hybrid wind farm parametrization (Pan and Archer, 2018).                                                                    5

The open-source Wind Farm Parameterization (WFP) of the Weather Research and Forecasting (WRF) model acts to collectively represent wind turbines in each model grid cell as a turbulence source and a momentum sink within the vertical levels of the turbine rotor disk (Fitch et al., 2012; Fitch, 2016). A fraction of the kinetic energy extracted by the virtual wind turbines is converted to power, reported as an aggregate sum in each model grid cell. The default setting of the WFP dictates that turbine-induced turbulence generation is derived from the difference between the thrust and power coefficients, though this option can      10 be switched off to constrain turbulent kinetic energy (TKE) to be added only via wind shear arising from the momentum deficit in the wake of the turbine. Wind-speed-dependent thrust coefficients specify the local wind drag on kinetic energy extraction as well as on power estimation. Users can modify the specifications of the parameterized turbine, such as its hub height, rotor diameter, power curve, and thrust coefficients, as well as its latitude and longitude location.

The WRF WFP has been employed in many studies with different model configurations to assess the impacts of onshore    15 and offshore wind farms (e.g. Eriksson et al. (2015); Jimenez et al. (2015); Miller et al. (2015); Vanderwende et al. (2016); Vanderwende and Lundquist (2016); Wang et al. (2019)). WFP simulations have reproduced the observed localized, nighttime, near-surface warming caused when wind turbines mix warmer air from the nocturnal inversion down to the surface (Fitch et al., 2013a, b; Lee and Lundquist, 2017b; Siedersleben et al., 2018a; Xia et al., 2019). Such findings have prompted additional studies using the WFP to address whether large-scale wind farms could alter regional climate (see Table 1 for an overview).   20 Specific examples include Vautard et al. (2014), who use WFP simulations of future European deployment at 50-km horizontal resolution and ∼30-m vertical resolution to find statistically significant temperature signals only in winter, constrained to ±0.3 K. Conversely, Pryor et al. (2018) use the WRF WFP at 4-km horizontal resolution and ∼30-m vertical resolution to find that wind farm-induced surface warming (<0.1 K on average) around wind farms in Iowa is more significant during summer months. Miller and Keith (2018), using WFP simulations at 30-km horizontal resolution and 25-m vertical resolution, suggest   25 that generating today's US electricity demand (which they estimate to be 0.46 $TW_e$) with only wind power would redistribute boundary-layer heat to warm the continental US (CONUS) surface temperatures by 0.24 K.

The varying WRF WFP configurations employed in previous wake studies present conflicting depictions of the impact of wind farm wakes, suggesting a sensitivity to model settings. Past studies have begun evaluating this sensitivity in the WRF WFP. Lee and Lundquist (2017a) note that a ∼12-m vertical resolution is necessary to reproduce observed power production,   30 while Mangara et al. (2019) find that the wake dynamics simulated by the WFP are more sensitive to horizontal resolution than vertical resolution. Xia et al. (2019) find differences in the WFP solution of surface temperature changes depending on the inclusion of the turbine-generated TKE term. Siedersleben et al. (2019) determine that a TKE source and a horizontal

**Table 1.** Overview of previous WRF WFP wake impact studies

| Reference | horizontal resolution[1] | vertical resolution[2] | near-surface temperature impact[3] |
|---|---|---|---|
| Fitch et al. (2013a) | 1 km | 15 m | increase of 0.5 K |
| Vautard et al. (2014) | 50 km | 30 m | wintertime changes ±0.3 K |
| Miller and Keith (2018) | 30 km | 25 m | increase of 0.24 K across CONUS |
| Pryor et al. (2018) | 4 km | 30 m | increase of <0.1 K |
| Siedersleben et al. (2018a) | 1.67 km | 35 m | increase of 0.4 K |
| Wang et al. (2019) | 1 km | 7 m | wintertime increase of 0.2 K |
| Xia et al. (2019) | 1 km | 20 m | increase of 0.3 K |

[1] Of innermost domain, if applicable
[2] Within rotor layer
[3] Within wind farm, unless otherwise specified

**Table 2.** Simulation configurations

| Identifier | horizontal resolution (dx) | vertical resolution (dz) | time step (dt) | TKE option | Computation time (CPU-hrs)[1] |
|---|---|---|---|---|---|
| dx03_dz10_dt30_tke | 3 km | 10 m | 30 s | Default | 200 |
| dx09_dz10_dt30_tke | 9 km | 10 m | 30 s | Default | 50 |
| dx27_dz10_dt30_tke | 27 km | 10 m | 30 s | Default | 12 |
| dx03_dz30_dt30_tke | 3 km | 30 m | 30 s | Default | 150 |
| dx03_dz10_dt30_ntke | 3 km | 10 m | 30 s | No added TKE | 200 |
| dx03_dz10_dt10_tke | 3 km | 10 m | 10 s | Default | 650 |
| dx01_dz10_dt30_ntke | 1 km | 10 m | 30 s | No added TKE | 630 |
| dx01_dz10_dt30_tke | 1 km | 10 m | 30 s | Default | 630 |

[1] Per one day (24 hours + 12 hour spin-up) of simulation. Domain sizes indicated in Fig. 1

resolution on the order of 5 km or finer are necessary to represent the impact of offshore wind farms on the stably stratified marine atmospheric boundary layer. While these studies give initial guidance on the sensitivity of the WFP to model settings, a greater breadth of spatial resolution and WFP TKE sensitivity tests are needed to formulate more confident best practice guidelines.

5    Here we expand upon and synthesize the work of Lee and Lundquist (2017a), Mangara et al. (2019), Xia et al. (2019), and Siedersleben et al. (2019) and provide guidance on optimal WRF WFP model settings for simulating wakes. Section 2 outlines the model set-up and configurations tested, Section 3 presents the differences in the configurations, and Sections 4 and 5 summarize our results confirming model sensitivity and recommend WRF WFP modeling choices.

## 2   Data and methods

10 ### 2.1   Observations

This sensitivity analysis relies on data from the Crop Wind Energy Experiment (CWEX). CWEX investigated the intersection of agriculture and wind energy within the planetary boundary layer (Rajewski et al., 2013). The site was characterized by

generally flat terrain and a vegetated surface of corn and soybeans and featured an operating wind farm northeast of the city of Ames, Iowa. In the 2013 CWEX campaign, seven surface flux stations, a radiometer, three profiling lidars, and a scanning lidar were deployed within and around this wind farm to explore the interaction of multiple wakes in a range of atmospheric stability conditions (Vanderwende et al., 2015; Bodini et al., 2017; Sanchez Gomez and Lundquist, 2019).

The WINDCUBE 200S scanning lidar was positioned within the northern half of the wind farm during CWEX-13, about 6 rotor diameters north of the nearest turbine row. The 200S lidar utilized a velocity azimuth display (VAD) scanning strategy that measured winds from ∼100 m to 4,800 m above ground level (AGL) approximately every 50 m. We use the 200S 75° elevation scans (Vanderwende et al., 2015) in this study to estimate horizontal winds every 30 min to validate the boundary-layer winds simulated by WRF.

We select August 24 through 27 of 2013 for our analysis. During this period, a lack of major synoptic events allowed strong nightly nocturnal low-level jets to occur (Vanderwende et al., 2015). Lee and Lundquist (2017a) found that WRF performed well in capturing the timing, intensity, and position of these low-level jets. Furthermore, the wind turbines operated without curtailment, and the instruments were online collecting data, making this period ideal for a model sensitivity and performance evaluation.

## 2.2 Modeling

We conduct the simulations comprising our sensitivity study with version 3.8.1 of the Advanced Research WRF (ARW) model (Skamarock and Klemp, 2008). While model time step, vertical resolution, and horizontal resolution (and thus domain size) are among the model settings varied to test sensitivity, several model options are kept consistent across all simulations based on previous studies of this time period. The 0.7° ERA-Interim (ECMWF, 2009; Dee et al., 2011) data set provides initial and boundary conditions for all model runs, and topographic data are provided at 30-s resolution. Physics options include the RRTM long-wave radiation scheme (Mlawer et al., 1997), the single-moment 5-class microphysics scheme (Hong et al., 2004), land surface physics with the Noah Land Surface Model (Ek et al., 2003), Dudhia short-wave radiation (Dudhia, 1989) with a 30-s time step, a surface layer scheme that accommodates strong changes in atmospheric stability (Jimenez et al., 2012), the MYNN2 PBL scheme (Nakanishi and Niino, 2006) *without* TKE advection, and the explicit Kain–Fritsch cumulus parameterization (Kain, 2004) on domains with horizontal resolutions coarser than 3 km.

We simulate each 24-hour day of August 24 through 27 individually, beginning spin-up at 1200 UTC on the previous day with analysis retained after 0000 UTC. We define the wake effect by comparing a simulation without the WFP to a simulation with the WFP, as in Fitch et al. (2012); Lee and Lundquist (2017a); Redfern et al. (2019). We use the power and thrust curve of the 1.5-MW PSU generic turbine (Schmitz, 2012) to parameterize the wind turbines, based on the General Electric SLE turbine (80-m hub height and 77-m rotor diameter). This turbine model closely matches those installed in the wind farm present at the CWEX site, and Siedersleben et al. (2018b) show little sensitivity to the exact turbine power curve.
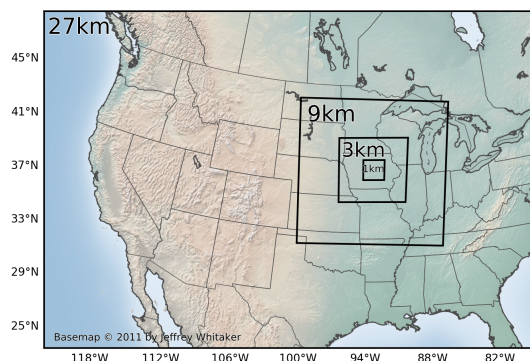
**Figure 1.** Map representing the domains of the horizontal resolution tests that also serve as the outer domains for finer resolutions. Geography data provided by Matplotlib's (Hunter, 2007) Basemap © 2011 by Jeffrey Whitaker.

We define a "baseline" configuration (*dx03_dz10_dt30_tke*) around which we modify various settings. This baseline is set to have three nested domains with horizontal resolutions of 27, 9, and 3 km, respectively, where the innermost, 3-km domain (*dx03*) covers the state of Iowa, centered over the simulated wind farm (Fig. 1). The vertical resolution of the baseline is nominally defined to be ∼10 m in the lowest 200 m (*dz10*), stretching vertically thereafter. The model time step is 30 s on the

5 outer domain (*dt30*), reducing by a factor of 3 for each additional nest. Turbine-induced turbulence is parameterized via an addition of TKE (*tke*), the default WFP option. We then vary the horizontal resolution (*dx*), vertical resolution (*dz*), time step (*dt*), and turbulence option (*tke* or *ntke*) about this baseline configuration to make up our sensitivity test (Table 2).

For example, we test vertical resolution sensitivity by comparing the baseline configuration to the *dx03_dz30_dt30_tke* configuration, which coarsens the vertical resolution from 10 m in the baseline to 30 m (*dz30*) and reduces the number of

10 layers intersecting the turbine rotor layer from ∼7 to 3 (Fig. 2). We test sensitivity to horizontal resolution by separately nesting higher resolution domains, first using only a 27-km domain, then adding a 9-km domain, a 3-km domain, and finally a 1-km domain (Fig. 1). Additionally, we test the impacts of the WFP turbine-generated TKE source by running two simulations with this option switched off (*dx03_dz10_dt30_ntke* and *dx01_dz10_dt30_ntke*). Finally, we examine sensitivity to model time step by running a simulation at a time step of 10 s on the outermost domain (*dx03_dz10_dt10_tke*), refined from 30 s in the other

15 configurations. Sensitivities of the tested configurations are determined via comparisons of model solutions of the wind farm wake, including the area of wake coverage and the magnitude of hub-height wind speed deficits and near-surface temperature changes. All simulation configurations are outlined in Table 2.
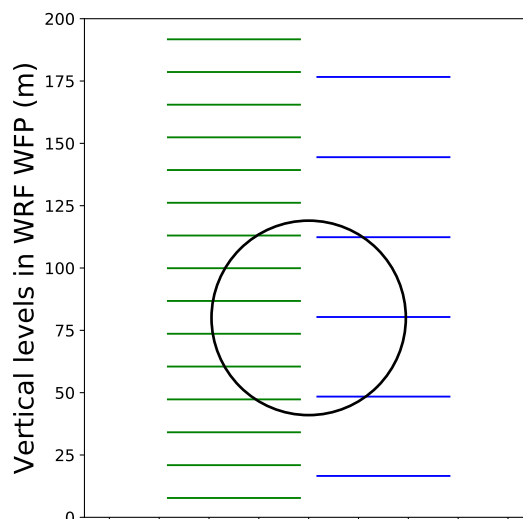
**Figure 2.** Schematic of the two vertical grids tested and where they typically intersect the turbine rotor layer (black circle): the ∼10-m grid (*dz10*) on the left in green and the ∼30-m grid (*dz30*) on the right in blue.

## 3 Results

### 3.1 Performance of non-WFP WRF

We first verify that the WRF simulations without the WFP, i.e. "no wind farm" (NWF) simulations, simulate accurate ambient winds compared to the CWEX scanning lidar measurements collected from outside the wind farm. Qualitatively, all WRF configurations in our sensitivity test have skill in simulating the timing and position of the LLJ (a similar finding of Smith et al. (2019)) but overestimate the magnitude of the LLJ wind speed increase (Fig. 3) and predict fewer occurrences of easterly winds, especially on August 24 and 25 (Fig. 4, not all configurations shown). We include time series of wind speed from two simulations, *dx27_dz10_dt30_tke* (Fig. 3a, Fig. 4a) and *dx01_dz10_dt30_tke* (Fig. 3b, Fig. 4b), as an example. The finer-horizontal resolution NWF *dx01_dz10_dt30_tke* better captures the intermittency in strength of the LLJ (Fig. 3a), though both simulations overestimate wind speed compared to the scanning lidar. Comparisons of the simulated near-hub-height hourly wind speed and direction against the scanning lidar further illustrate the positive wind speed bias (Fig. 5a) and more easterly wind direction bias (Fig. 5b) by the simulations, with the 27-km horizontal resolution simulation showing higher biases than the 1-km in both cases. The RMSE differences between the 27-km and 1-km configurations are small in the wind speed estimates (3.9 m s$^{-1}$ vs. 3.8 m s$^{-1}$, respectively), but differ more in the wind direction estimates, with the 27-km configuration exhibiting an RMSE of 67.4° compared to the 1-km RMSE of 53.6°. Evaluation of other heights (150 m and 200 m, not shown) reveal a similar pattern of higher biases in the 27-km domain than the 1-km, particularly in wind direction.
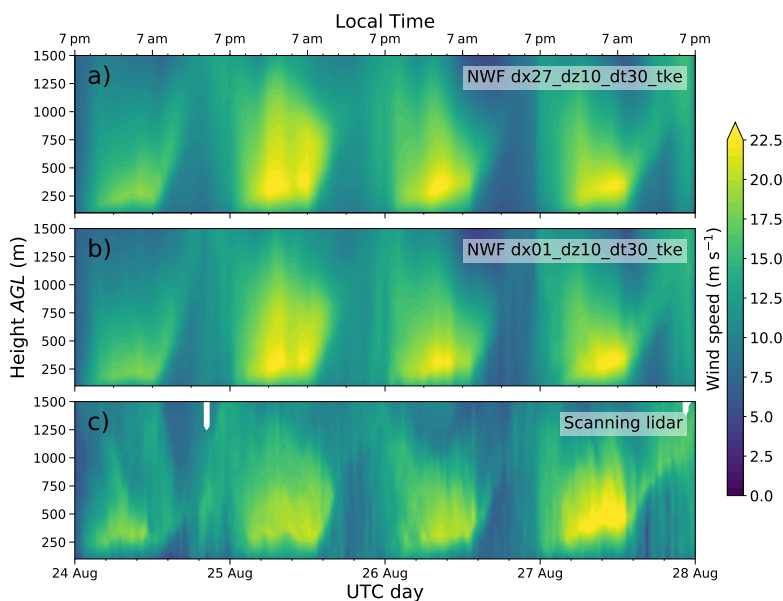
**Figure 3.** Time-height cross-sections comparing wind speed from a) the no wind farm (NWF) run of the *dx27_dz10_dt30_tke* simulation with b) the NWF run of *dx01_dz10_dt30_tke* and c) the scanning lidar observations.

Our comparisons of NWF simulations and scanning lidar measurements are similar to those of Lee and Lundquist (2017a), who also found good agreement in the occurrence of the LLJ. Lee and Lundquist (2017a) noted slightly better agreement in LLJ strength between simulations and the scanning lidar (i.e. an absolute error on the order of 1 m s$^{-1}$), which may be related to the larger domain sizes of their simulations.

### 3.2 WRF WFP sensitivity to model settings

#### 3.2.1 Impact on hub-height wind speed deficits

For an initial qualitative assessment of WRF WFP sensitivity to model settings, we compare snapshots of the wake effect at a single point in time among the various model configurations by subtracting the NWF simulation from the WFP simulation. We select 0200 UTC of August 26 (2100 Aug 25 local time) to examine due to the presence of strong southwesterly LLJ winds within and above the turbine rotor layer and the easily discernible wake impacts across all configurations tested, though many other time periods could have provided a similarly qualitative comparison.

The baseline simulation on 0200 Aug 26 (Fig. 6a) shows a clear hub-height wind speed deficit downwind of the wind farm, its impact extending over 40 km downwind with a maximum wind speed deficit close to 1.5 m s$^{-1}$. Changing the horizontal resolution of the WRF WFP reveals a clear sensitivity. Configurations with a coarser horizontal grid spacing predict wind speed deficits smaller in magnitude than the baseline, but spanning a larger area (Fig. 6a,b). Conversely, a finer horizontal resolution
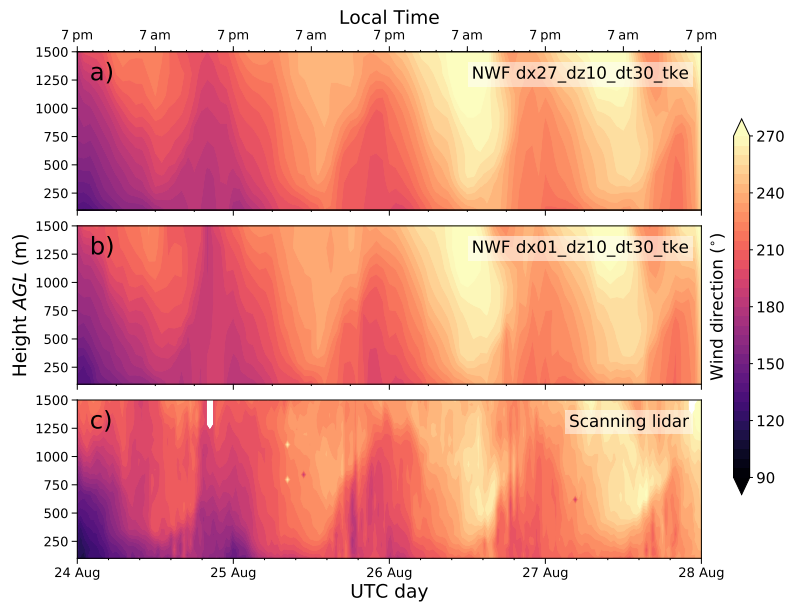
**Figure 4.** Time-height cross-sections comparing wind direction from a) the no wind farm (NWF) run of the *dx27_dz10_dt30_tke* simulation with b) the NWF run of *dx01_dz10_dt30_tke* and c) the scanning lidar observations.
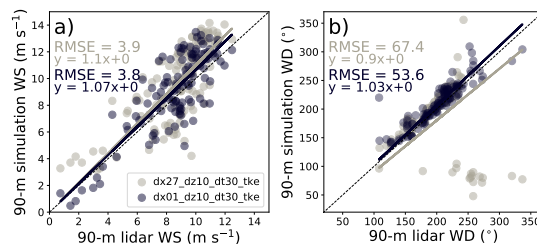
**Figure 5.** Hourly values of 90-m a) wind speed (WS) and b) wind direction (WD) from two of the simulations tested plotted against those of the scanning lidar. Dots, lines of best fit, and their corresponding equations and RMSE calculations in both panels are colored based on the model configuration denoted in the legend in panel (a). One-to-one lines are dashed in black.

(Fig. 6h) reduces the area of impact but increases the magnitude of the wind speed deficit. Coarsening the near-surface vertical resolution from 10 m in the baseline simulation to 30 m impacts the model solution by changing the shape of the wind speed deficit region (Fig. 6d). Disabling the WFP turbine-generated TKE option also only slightly impacts the shape of the wind speed deficit although has negligible impacts on its magnitude (Fig. 6e), regardless of horizontal grid spacing (Fig. 6g,h).

To explicitly quantify differences between the tested configurations, we sum the total area impacted by a particular magnitude of waking impact (e.g. wind speed deficit) in hourly increments. For example, the area impacted by an 80-m wind speed deficit of 1 m s$^{-1}$ in the baseline simulation on Aug 26 at 0200 UTC (Fig. 6a) is calculated to be about 80 km (denoted at the

dashed black line in Fig. 7). We repeat the calculation for several defined deficits of interest for each hour in the period for all simulations (Fig. 7).

This time series of wake impact areas gives insight on the temporal variability of waking, as we see the largest areas of impact (larger dots in Fig. 7) and the strongest magnitudes of deficit occur during the night, with little to no wake impact

5 areas present during the day when increased ambient turbulence erodes wakes, similar to the stability dependence highlighted in Lundquist et al. (2018). As expected, all simulations exhibit larger areas impacted by lower deficit magnitudes (0.4−0.6 m s$^{-1}$) relative to instances of stronger deficits (>1 m s$^{-1}$). Clear differences emerge in the details of wake area coverage between the model configurations, especially when horizontal resolution is varied (Fig. 7a). As the horizontal resolution is coarsened from 1 km (dark purple), to 3 km (green), to 9 km (pink), and finally to 27 km (gray), the simulation increasingly

10 fails to capture higher-magnitude wake impacts and instead predicts larger areas of minor deficits.

The spatial extent of wind speed deficit impact appears to be most sensitive to horizontal resolution, and is less sensitive to the other model settings tested (Fig. 7b). Holding horizontal resolution constant and reducing the model time step (blue) or disabling the WFP turbulence generation (light purple) does not cause significant changes to the simulations' wind speed deficit extent across the range of impact magnitudes examined. The simulation with coarse vertical grid spacing (yellow) differs

15 most from the others in Fig. 7b, predicting slightly larger regions of relatively weaker wake impacts, following the trend of the coarser horizontal resolution simulations.

We next integrate the areas impacted by each defined deficit value in time across the full period (Fig. 8) to corroborate earlier suggestions of sensitivity to model configuration in Figs. 6 and 7. The coarser horizontal grid spacing simulations predict the largest overall region, with weaker wind speed deficits than the finer grid spacing simulations. Additionally, the

20 coarse vertical resolution simulation produces smaller regions of strong wake impacts (>1.6 m s$^{-1}$ deficits) compared to its finer vertical resolution counterparts. Throughout the range of waking magnitudes, the original baseline simulation (3-km horizontal resolution, green) closely matches the fine-resolution (1 km) simulation's estimates of wake coverage, suggesting WRF WFP estimates of wake impact and spatial coverage begin to converge at 3-km horizontal grid spacing (Fig. 8). Disabling the WFP TKE term has minimal impact between the two 1-km (red vs. dark purple) and two 3-km (light purple vs. green)

25 simulation pairs examined when considering wind speed deficit effects. Differences between the baseline's 30-s time step and the reduced, 10-s time step simulation (blue) are small (Fig. 8).

### 3.2.2   Impact on near-surface temperature and moisture changes

Another wind farm wake effect sensitive to WRF WFP model settings is the presence and sign of near-surface temperature changes. As with the wind speed deficit analysis (Fig. 6), initial comparisons of snapshots of the temperature changes on August

30 26 at 0200 UTC reveal differences between the configurations (Fig. 9, 10). The baseline simulation shows a clear nighttime warming signal at 2 m in the immediate vicinity of the wind turbines (Fig. 9a), consistent with satellite observations (Zhou et al., 2012) and in situ observations (Rajewski et al., 2013). This warming is caused by a redistribution of heat mixed down

from hub-height (Fig. 10a), as shown by a concurrent vertical slice transecting south-north through the wind farm (dashed line in Fig. 9a). Changing the horizontal resolution of the WRF WFP has a notable impact on the spatial coverage of the near-surface warming. Simulations with coarser horizontal resolutions predict weaker 2-m temperature warming signals that span greater areas (Fig. 9b,c; 10b,c), which parallels results from the wind speed deficit analysis (Fig. 6b,c). Similarly, reducing the time step has little impact on the model solution of temperature changes (Fig. 9h, 10f). 5

Changes to turbine-generated turbulence and vertical resolution exert the greatest impacts on model solutions of temperature signals. Coarsening the vertical grid spacing from 10 m to 30 m reverses the sign of the near-surface temperature change, producing an unphysical localized region of surface cooling in the immediate vicinity of the wind farm (Fig. 9d, 10d). Similarly, disabling turbine-generated turbulence also causes a cooling signal near the surface, irrespective of horizontal resolution (Fig. 9e,g; 10e,g). Temperature profiles from these configurations reveal slight warming within grid cells at turbine hub-height 10 that does not mix down to the surface (Fig. 10d,e,g). This cooling signal produced by simulations with too-coarse vertical resolution or lacking turbine-generated TKE directly conflicts with wind farm wake observations of localized near-surface warming during stable conditions (e.g. Zhou et al. (2012); Rajewski et al. (2013)). All configurations produce cooling just above turbine hub-height and warming within the rotor layer, illustrating the redistribution of heat that occurs due to mixing of the nocturnal inversion; however, sufficient vertical resolution and turbine-generated turbulence is required to mix warmer 15 temperatures down to the surface (Fig. 10).

We sum at hourly increments the total area impacted by a particular magnitude of near-surface temperature change to explicitly quantify differences between tested configurations (Fig. 11). We limit the bounding area of interest to grid cells immediately around the wind farm to consider the more localized nature of near-surface temperature impacts, as opposed to the larger downwind fetch impacted by a wind speed deficit considered in Fig. 7. The temporal variability of waking again 20 appears, with relatively larger areas of temperature impacts occurring overnight, typically emerging as a warming signal. These temperature impacts are clearly sensitive to horizontal grid spacing throughout the time period (Fig. 11a). As the horizontal resolution is coarsened from 1 km (dark purple), to 3 km (green), to 9 km (pink), and finally to 27 km (gray), the simulation predicts larger areas of minor deficits and fails to capture higher-magnitude temperature increases. Occasional instances of cooling occur typically just before sunset and are exaggerated in coarser horizontal resolution configurations likely due to 25 convection in the daytime with locations shifted due to the presence of the wind farm.

Coarsening vertical resolution to 30 m (yellow) or disabling TKE generation (light purple) incorrectly produces a nocturnal cooling signal across the time period (Fig. 11b), most notably on Aug 25 through 27. WRF WFP needs to be able to resolve wind shear to vertically mix warmer inversion air to the the surface as documented in observations (e.g. Rajewski et al. (2013); Smith et al. (2013); Rajewski et al. (2016); Platis et al. (2018); Siedersleben et al. (2018a)), and these configurations with 30 too-coarse vertical grid spacing (30 m) or lacking turbine-generated TKE clearly fail to generate such wind shear throughout most of the period. An exception occurs on Aug 24, when more southeasterly winds (Fig. 4) aligning with the orientation of the wind farm cause a narrow, highly concentrated wake region that permits the 30-m vertical resolution configuration to

produce a surface warming signal. While WRF WFP wake effects experience strong sensitivity to vertical resolution and TKE generation, reducing the model time step (blue) from the baseline (green) has little impact on the temperature change solution throughout the period (Fig. 11b).

As with the wind speed deficit analysis, we next integrate the areas impacted by each defined deficit value in time across the full period (Fig. 12), which reiterates that significant model sensitivities emerge. The configurations without turbine-generated turbulence at both 1-km and 3-km horizontal resolutions (red, purple, respectively) or with a coarse, 30-m vertical resolution (yellow), exhibit the largest erroneous overall areas of significant cooling signals in the vicinity of the wind farm (Fig. 12). The 9-km horizontal resolution (pink) also experiences relatively stronger cooling impacts across the period, but estimates total areas impacted by warming to span hundreds of kilometers more. Other configurations that experience cooling with adequate (10-m) vertical grid spacing and the turbine-TKE enabled estimate such cooling to be minimal in total coverage and magnitude (Fig. 12).

All configurations predict some warming immediately around the wind farm throughout the period (Fig. 12), while those with the 30-m vertical grid or lacking turbine-generated TKE produce the smallest areas of warming. Configurations with the coarsest horizontal resolutions (27 km, grey; 9 km, pink) predict large areas of impact by weak warming signals. Only configurations with a 3-km or finer horizontal grid are able to capture warming impacts above 0.4 K. Reducing model time step (blue) again has little impact on the overall prediction of temperature impact coverage compared to the baseline (green) (Fig. 12).

Another impact of wind farm wakes is the changes to the near-surface moisture content, when can happen overnight when the enhanced mixing from the wind farm brings relatively drier air down and moister air up, leading to a drying near the surface and moistening aloft (Baidya Roy, 2004; Siedersleben et al., 2018a). We examine the model sensitivity in producing this moisture effect via a vertical snapshot of water vapor mixing ratio (q) changes on August 26 at 0200 UTC (Fig. 13). As with the temperature analysis (Fig. 10), changing the horizontal resolution of the WRF WFP has a notable impact on the spatial coverage and intensity of the near-surface drying. Simulations with coarser horizontal resolutions predict weaker near-surface drying signals that span larger areas (Fig. 13b,c).

However, changes to turbine-generated turbulence and vertical resolution have the greatest impacts on model solutions of moisture signals. Coarsening the vertical grid spacing from 10 m to 30 m reverses the sign of the moisture change, producing a localized region of surface moistening in the immediate vicinity of the wind farm (Fig. 13d). Similarly, disabling turbine-generated turbulence also causes an increase in water vapor near the surface, irrespective of horizontal resolution (Fig. 13e,g). This moistening signal produced by simulations with too-coarse vertical resolution or lacking turbine-generated TKE contradicts observations of localized near-surface drying during stable conditions (Baidya Roy, 2004; Siedersleben et al., 2018a), implying that those simulations lack sufficient mixing, the same deficiency that produces erroneous cooling signals (Fig. 10) as well. We omit discussing the model sensitivity in producing moisture impacts with the same detail as the temperature changes, as the moisture impact results parallel those of the temperature impacts.
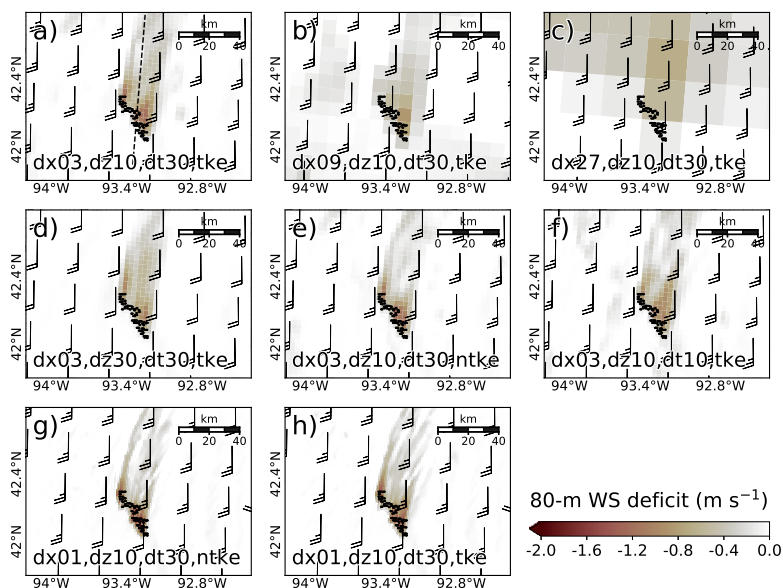
**Figure 6.** Hub-height (∼ 80 m) wind speed (WS) deficits resulting from the presence of the wind farm in the tested simulations on Aug 26 0200 UTC (Aug 25 2100 LT). 80-m wind barbs from the wind farm simulation are plotted in knots every 27 km, regardless of horizontal resolution. The dashed line in panel a denotes the location of the vertical cross-section in Fig. 10. Panels are cropped to the same region around the wind farm despite certain configurations having varying simulation domains depending on horizontal resolution.

## 4   Discussion

We compare different WRF WFP simulation solutions of onshore wind farm wake effects in simple terrain and meteorological conditions to quantify the sensitivity of the simulations to model configuration and thereby define recommendations for best-practice model settings. Settings tested include horizontal and vertical grid spacing, model time step, and inclusion of turbine-generated turbulence. We divide our analysis into the two main atmospheric impacts of a wind farm wake: a hub-height wind speed deficit extending downwind of the wind farm and a nighttime near-surface temperature increase immediately around the wind farm mixed down from the nocturnal inversion.

   In summary, simulated WRF WFP solutions of wind speed deficits are most sensitive to the horizontal resolution. Horizontal grids of 3-km and 1-km converged on similar depictions of the magnitude and spatial coverage of wind deficits, while grids of 9-km or larger dilute the wake impact over large areas. Solutions of 2-m temperature (and similarly moisture) changes are also sensitive to horizontal resolution in that too-coarse (>9 km) grid spacing results in large expanses of weak temperature changes, contradicting the typically localized nature of temperature impacts from a wind farm seen in observations (e.g. Baidya Roy (2004); Zhou et al. (2012); Rajewski et al. (2013); Siedersleben et al. (2018a)). The more important model settings to consider for accurate representation of surface temperature impacts of wind farm wakes, however, are the vertical resolution and turbine-
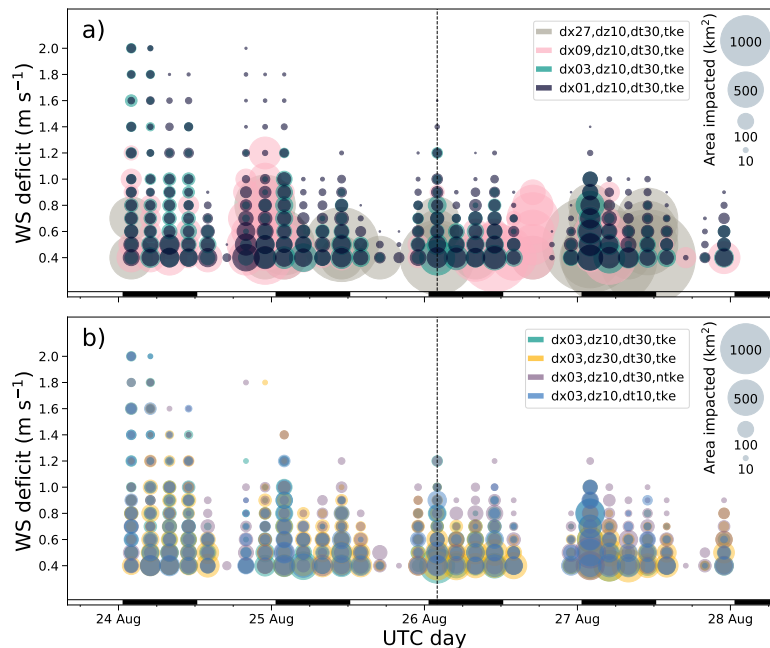
**Figure 7.** Time series of area impacted by the wake-induced 80-m wind speed deficits as predicted by the tested simulations, plotted every 3 hours throughout the period. The size of the dots represents the spatial coverage of their respective magnitude of impact (scale denoted in top right), with each dot colored based on its configuration. Areas of impact were calculated for deficits every 0.1 m s$^{-1}$ between 0.4 and 1.0 m s$^{-1}$, then every 0.2 m s$^{-1}$ until 2.0 m s$^{-1}$. The configurations are divided into groups that a) vary horizontal resolution and b) hold horizontal resolution constant and vary other model settings. The time chosen for the qualitative analysis (Aug 26 0200 UTC) in Fig. 6 is denoted by the black dashed line. Black and white bar at bottom denotes post-sunrise (white) and post-sunset (black).
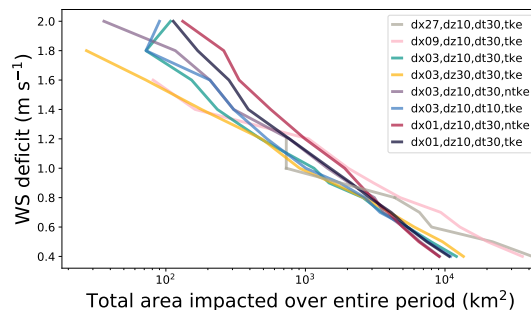
**Figure 8.** Total area impacted by the wake-induced 80-m wind speed deficits as predicted by the tested simulations, plotted at different magnitudes of impact and integrated in time across the entire period. Each line is colored based on its configuration.

generated turbulence term, as a too-coarse (i.e. 30 m) vertical grid or a lack of additional turbine turbulence fails to simulate enough wind shear to vertically mix warm inversion air to the surface, resulting in an incorrect surface cooling signal overnight.

Out of the four horizontal resolutions tested, the finer-grid (1-km and 3-km) configurations produce a more robust representation of wind farm wakes compared to the coarser grids (9 km and 27 km). The finer grid spacing allows stronger wake
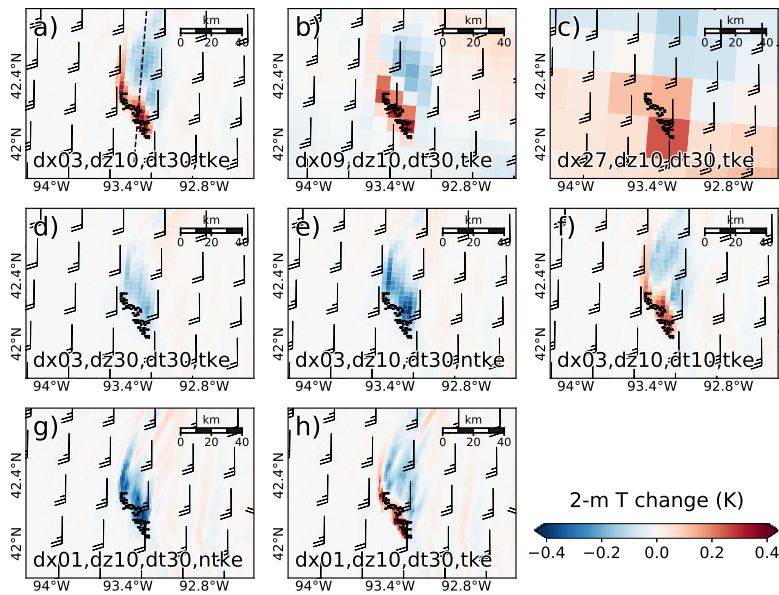
**Figure 9.** Near-surface (2 m) temperature (T) changes resulting from the presence of the wind farm in the tested simulations on Aug 26 0200 UTC (Aug 25 2100 LT). 80-m wind barbs from the wind farm simulation are plotted in knots every 27 km, regardless of horizontal resolution. The dashed line in panel a denotes the location of the vertical cross-section in Fig. 10. Panels are cropped to the same region around the wind farm despite certain configurations having varying simulation domains depending on horizontal resolution.
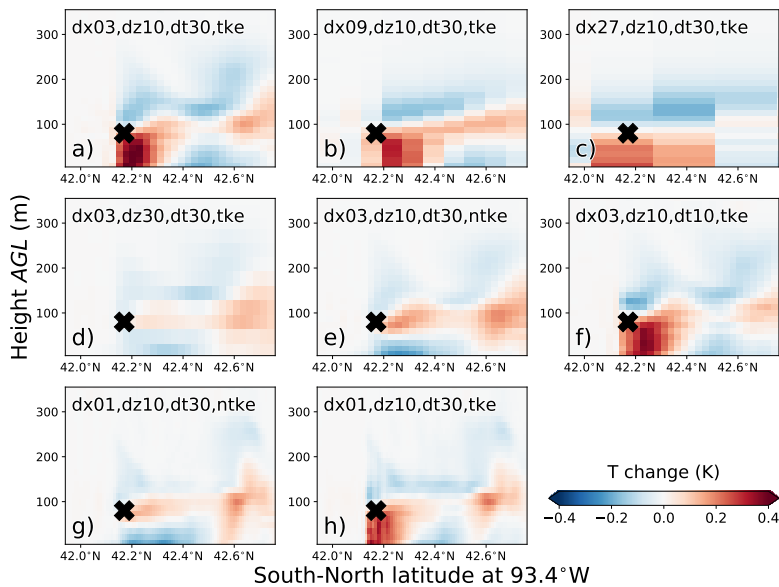
**Figure 10.** Vertical cross-sections of temperature (T) changes resulting from the presence of the wind farm in the tested simulations on Aug 26 0200 UTC (Aug 25 2100 LT). The median location and hub-height of the wind farm is denoted by the black X. Location of this slice is denoted by the dashed line in Fig. 9.
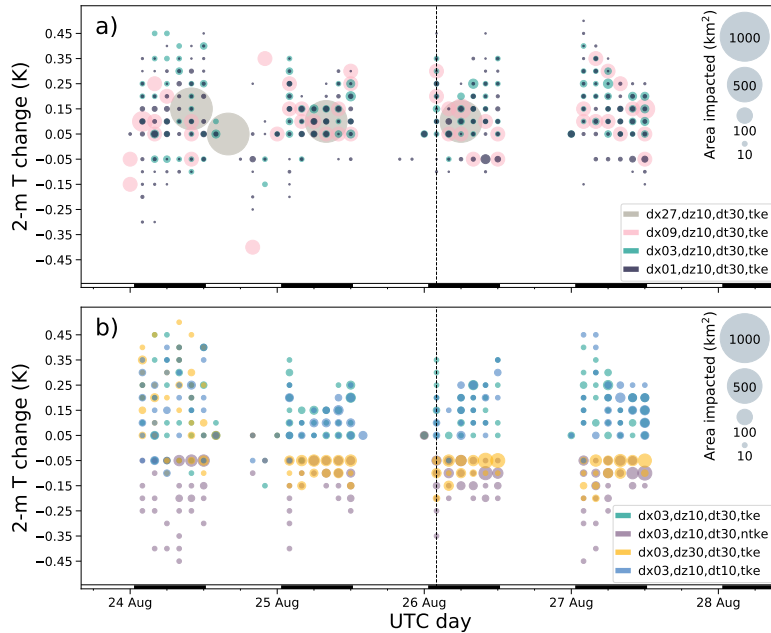
**Figure 11.** Time series of area impacted by the wake-induced 2-m temperature changes as predicted by the tested simulations, plotted every 2 hours throughout the period. The size of the dots represents the spatial coverage of their respective magnitude of impact (scale denoted in top right), with each dot colored based on its configuration. The configurations are divided into groups that a) vary horizontal resolution and b) hold horizontal resolution constant while varying other model settings. The time chosen for the qualitative analysis (Aug 26 0200 UTC) in Fig. 6 is denoted by the black dashed line. Black and white bar at bottom denotes post-sunrise (white) and post-sunset (black).
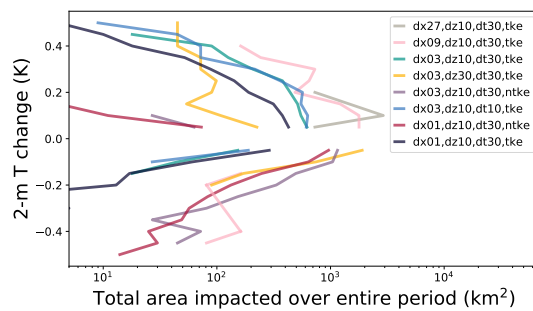
**Figure 12.** Total area impacted by the wake-induced 2-m temperature change as predicted by the tested simulations, plotted at different magnitudes of impact and integrated in time across the entire period. Each line is colored based on its configuration. Areas of warming are summed separately from areas of cooling.

impacts both in the wind speed deficit and surface warming to develop over a more localized region, better matching observations (e.g. Siedersleben et al. (2018a)). Coarser horizontal grids (>9 km) have been chosen in recent work (e.g. Vautard et al. (2014); Miller and Keith (2018)) for long-term or spatially large simulations because of the savings in computational expenses (see Table 2). However, such simulations imply a broader region of impact than realistic (Fig. 6, 7, 8). Configurations on the order of a few kilometers in the innermost, turbine-containing domain are thus recommended. Close similarities between the
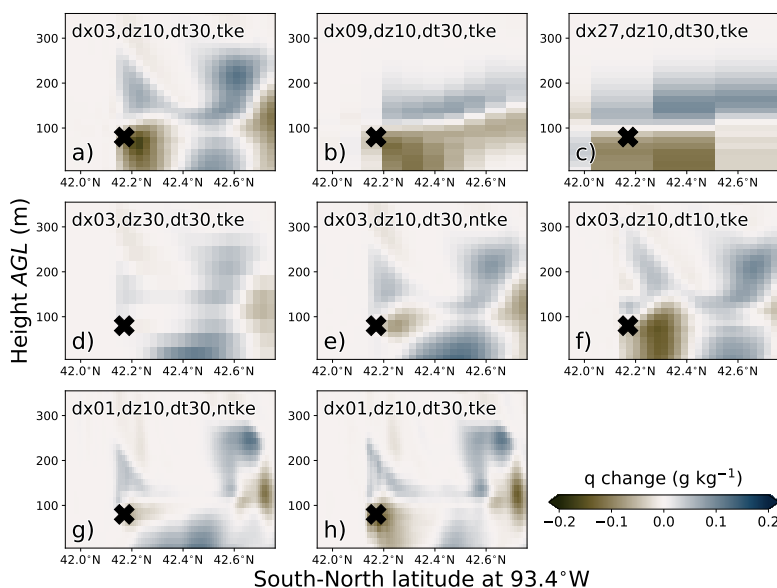
**Figure 13.** Vertical cross-sections of water vapor mixing ratio ($q$) changes resulting from the presence of the wind farm in the tested simulations on Aug 26 0200 UTC (Aug 25 2100 LT). The median location and hub-height of the wind farm is denoted by the black X. Location of this slice is denoted by the dashed line in Fig. 9.

1-km and 3-km configurations suggest the user can confidently produce accurate waking with a 3-km WRF WFP grid spacing, refining to 1 km if the computation resources are available or if terrain complexity indicates that finer resolution is required.

The choice of vertical resolution significantly impacts WRF WFP solutions of wake effects, especially in the representation of nocturnal near-surface warming around the wind farm (Fig. 9d, 10d, 11b, 12). A 30-m vertical grid consistently produces incorrect cooling signals overnight compared to the baseline simulation with a 10-m grid. Observed surface warming in the vicinity of wind farms occurs because of the turbine-generated turbulence mixing down warm air from above the nighttime inversion to the surface (Baidya Roy, 2004; Baidya Roy and Traiteur, 2010; Zhou et al., 2012; Rajewski et al., 2013). A sufficiently refined vertical grid is thus necessary to resolve this downward mixing, and a 30-m grid is inadequate. These findings support prior work by Lee and Lundquist (2017a), who also conclude that a finer (∼12 m) vertical grid is favorable for the separate purpose of producing more accurate WRF WFP solutions of the winds and power production compared to a coarser (∼22 m) grid. However, coarse (>20 m) vertical resolutions have been employed in other past WRF WFP studies, possibly artificially constraining the temperature signal (e.g. occurrence of both negative and positive temperature signals seen in Vautard et al. (2014)).

In addition, the turbine-induced turbulence option has similar impacts on the WRF WFP wake solution as the vertical resolution. When enabled, this turbulence option within the WFP adds an additional source of TKE within turbine-containing grid cells derived from the difference between the turbine thrust and power coefficients. Without this added TKE source, WRF wind farm wake turbulence only develops due to the wind shear that arises out of the momentum deficit aloft in the wind farm

wake. However, this shear-induced mixing is insufficient, as configurations without the added turbine-TKE option consistently produce inaccurate nocturnal cooling signals at the surface immediately beneath the wind farm (Fig. 9e,g 10e,g 11b, 12). Such surface cooling implies that insufficient mixing is occurring within WRF WFP, making it unable to bring warm inversion air to the surface. This hypothesis is corroborated by Xia et al. (2019), who demonstrated that the WFP turbulence option is

5 responsible for the surface warming signal through the enhancement of vertical mixing. As such, the WFP turbine TKE option, in addition to sufficiently refined vertical and horizontal grid resolutions (∼10 m and ∼3 km, respectively), is required in order to represent wind farm wakes accurately.

## 5   Conclusions

As wind energy continues to rapidly develop, the Wind Farm Parameterization (WFP) within the Weather Research and Fore-

10 casting (WRF) model (version 3.8.1) provides a means for simulating wind farms and their meteorological wake effects. However, little guidance currently exists for choice in model settings to produce the most accurate solution of wakes. Herein, we assess the sensitivity of the WRF WFP to model configuration to provide recommended settings for simulating wind farm wakes effects.

We select August 24-27 of the 2013 Crop Wind Experiment (CWEX-13) field campaign as our case study due to the simple

15 terrain, availability of observations, and consistent nocturnal low-level jet occurrences without interference from large-scale synoptic meteorological events. We use measurements from a scanning lidar to first verify the ambient flow simulated by WRF before implementing the WFP and varying the horizontal and vertical resolutions, turbine-generated turbulence, and model time step settings to comprise the sensitivity analysis. Each model configuration simulates a real Iowa wind farm containing 200 1.5 MW turbines.

20 We isolate the impacts of WRF WFP settings on the two predominant meteorological effects of a wind farm wake, the hub-height wind speed deficit and the transient surface temperature increase arising out of downward mixing of the nocturnal inversion. While the inclusion of the turbine-generated turbulence option in the WFP has little impact on the wind speed deficit solution, disabling it results in an inaccurate cooling signal beneath the wind farm. Similarly, a coarse (30 m) vertical resolution has minimal impact on the representation of the wind deficit aloft, but impacts the surface temperature signal drastically by

25 reversing the sign of the expected temperature impact. WRF WFP simulations thus require a ∼10-m low-level vertical grid as well as the turbine-turbulence option enabled to produce the wind shear necessary to vertically mix the inversion air and attain the expected surface warming and drying. Horizontal resolution affects both the wind speed deficit and surface warming: a too-coarse (>9 km) grid dilutes wake effect intensity over greater areas, while grids of 1 km or 3 km converge on similar depictions of the magnitude and spatial coverage of wake impacts and thus serve as our recommended horizontal grid choice.

30 In conclusion, the WRF WFP is sensitive to certain model settings, particularly 1) the horizontal resolution in producing accurate intensity and coverage of the wind speed deficit and surface temperature change; and 2) the vertical resolution and 3)

turbine turbulence option in producing the correct surface warming signal. In order to obtain the most accurate representation of wind farm wakes, we suggest that users define a horizontal grid for the turbine-containing domain on the order of a few kilometers and a vertical grid near 10 m in the lowest ∼200 m. The inclusion of turbine-generated turbulence is also necessary.

This sensitivity study and subsequent model setting recommendations are derived from analysis of a single location and time period, and further analysis including a wider range of meteorological conditions or locations could be worthwhile, especially as wind energy develops more offshore and in complex terrain onshore. While we predict the WFP wake solutions and model sensitivity in less-turbulent offshore environments will behave similarly to the simple terrain case studied herein, the more-turbulent flow over complex topography may alter how wakes are represented in the WRF WFP and thus impact the model sensitivity. Furthermore, within-the-grid-cell turbine wake interactions are omitted in the WFP and not considered here. Future applications of the WRF WFP to investigate wind farm wake effects will have scientific and societal implications, so it is therefore important to consider model settings when designing simulations.

*Code and data availability.* The WRF-ARW model code (https://doi.org/doi:10.5065/D6MK6B4K) is publicly available at http://www2.mmm.ucar.edu/wrf/users/. This work uses the WRF-ARW model and the WRF Preprocessing System (WPS) version 3.8.1 (released on 12 August, 2016), and the wind farm parameterization is distributed therein. Initial and boundary conditions are provided by Era-Interim (Dee et al., 2011) available at https://rda.ucar.edu/datasets/ds627.0/. Topographic data are provided at 30-s resolution from http://www2.mmm.ucar.edu/wrf/users/download.html. The PSU generic 1.5 MW turbine (Schmitz, 2012) is available at https://doi.org/10.13140/RG.2.2.22492.18567. The user input and data needed to recreate the figures and analysis are located at https://doi.org/10.5281/zenodo.3478574.

*Author contributions.* JKL and JMT conceived the research and designed the WRF simulations; JMT carried out the WRF simulations and wrote the manuscript with significant input from JKL.

*Competing interests.* The authors declare that they have no competing interests.

*Acknowledgements.* This work and JMT were supported by an NSF Graduate Research Fellowship under grant number 1144083. WRF simulations were conducted using the Extreme Science and Engineering Discovery Environment (XSEDE), which is supported by National Science Foundation grant number ACI1053575. JKL's effort was supported by an agreement with NREL under APUP UGA-0-41026-65.

## References

Abkar, M. and Porté-Agel, F.: Influence of atmospheric stability on wind-turbine wakes: A large-eddy simulation study, Physics of Fluids, 27, 035 104, https://doi.org/10.1063/1.4913695, 2015a.

Abkar, M. and Porté-Agel, F.: A new wind-farm parameterization for large-scale atmospheric models, Journal of Renewable and Sustainable Energy, 7, 013 121, https://doi.org/10.1063/1.4907600, 2015b.

Aitken, M. L., Kosović, B., Mirocha, J. D., and Lundquist, J. K.: Large eddy simulation of wind turbine wake dynamics in the stable boundary layer using the Weather Research and Forecasting Model, Journal of Renewable and Sustainable Energy, 6, 033 137, https://doi.org/10.1063/1.4885111, 2014.

Archer, C. L., Mirzaeisefat, S., and Lee, S.: Quantifying the sensitivity of wind farm performance to array layout options using large-eddy simulation, Geophysical Research Letters, 40, 4963–4970, https://doi.org/10.1002/grl.50911, 2013.

Baidya Roy, S.: Can large wind farms affect local meteorology?, Journal of Geophysical Research, 109, D19 101, https://doi.org/10.1029/2004JD004763, 2004.

Baidya Roy, S. and Traiteur, J. J.: Impacts of wind farms on surface air temperatures, Proceedings of the National Academy of Sciences, 107, 17 899–17 904, https://doi.org/10.1073/pnas.1000493107, 2010.

Barrie, D. B. and Kirk-Davidoff, D. B.: Weather response to a large wind turbine array, Atmospheric Chemistry and Physics, 10, 769–775, https://doi.org/10.5194/acp-10-769-2010, 2010.

Bodini, N., Zardi, D., and Lundquist, J. K.: Three-dimensional structure of wind turbine wakes as measured by scanning lidar, Atmospheric Measurement Techniques, 10, 2881–2896, https://doi.org/10.5194/amt-10-2881-2017, 2017.

Calaf, M., Meneveau, C., and Meyers, J.: Large eddy simulation study of fully developed wind-turbine array boundary layers, Physics of Fluids, 22, 015 110, https://doi.org/10.1063/1.3291077, 2010.

Christiansen, M. B. and Hasager, C. B.: Wake effects of large offshore wind farms identified from satellite SAR, Remote Sensing of Environment, 98, 251–268, https://doi.org/10.1016/j.rse.2005.07.009, 2005.

Churchfield, M. J., Lee, S., Michalakes, J., and Moriarty, P. J.: A numerical study of the effects of atmospheric and wake turbulence on wind turbine dynamics, Journal of Turbulence, 13, https://doi.org/10.1080/14685248.2012.668191, 2012.

Dee, D. P., Uppala, S. M., Simmons, A. J., Berrisford, P., Poli, P., Kobayashi, S., Andrae, U., Balmaseda, M. A., Balsamo, G., Bauer, P., Bechtold, P., Beljaars, A. C. M., van de Berg, L., Bidlot, J., Bormann, N., Delsol, C., Dragani, R., Fuentes, M., Geer, A. J., Haimberger, L., Healy, S. B., Hersbach, H., Hólm, E. V., Isaksen, L., Kållberg, P., Köhler, M., Matricardi, M., McNally, A. P., Monge-Sanz, B. M., Morcrette, J.-J., Park, B.-K., Peubey, C., de Rosnay, P., Tavolato, C., Thépaut, J.-N., and Vitart, F.: The ERA-Interim reanalysis: configuration and performance of the data assimilation system, Quarterly Journal of the Royal Meteorological Society, 137, 553–597, https://doi.org/10.1002/qj.828, 2011.

Dudhia, J.: Numerical Study of Convection Observed during the Winter Monsoon Experiment Using a Mesoscale Two-Dimensional Model, Journal of the Atmospheric Sciences, 46, 3077–3107, https://doi.org/10.1175/1520-0469(1989)046<3077:NSOCOD>2.0.CO;2, 1989.

ECMWF: ERA-Interim Project, Research Data Archive at the National Center for Atmospheric Research, Computational and Information Systems Laboratory, Boulder CO, https://doi.org/10.5065/D6CR5RD9, 2009.

Ek, M. B., Mitchell, K. E., Lin, Y., Rogers, E., Grunmann, P., Koren, V., Gayno, G., and Tarpley, J. D.: Implementation of Noah land surface model advances in the National Centers for Environmental Prediction operational mesoscale Eta model, Journal of Geophysical Research: Atmospheres, 108, 2002JD003 296, https://doi.org/10.1029/2002JD003296, 2003.

Emeis, S.: A simple analytical wind park model considering atmospheric stability, Wind Energy, 13, 459–469, https://doi.org/10.1002/we.367, 2009.

Emeis, S. and Frandsen, S.: Reduction of horizontal wind speed in a boundary layer with obstacles, Boundary-Layer Meteorology, 64, 297–305, https://doi.org/10.1007/BF00708968, 1993.

Eriksson, O., Lindvall, J., Breton, S.-P., and Ivanell, S.: Wake downstream of the Lillgrund wind farm - A Comparison between LES using the actuator disc method and a Wind farm Parametrization in WRF, Journal of Physics: Conference Series, 625, 012 028, https://doi.org/10.1088/1742-6596/625/1/012028, 2015.

Fitch, A. C.: Climate Impacts of Large-Scale Wind Farms as Parameterized in a Global Climate Model, Journal of Climate, 28, 6160–6180, https://doi.org/10.1175/JCLI-D-14-00245.1, 2015.

Fitch, A. C.: Notes on using the mesoscale wind farm parameterization of Fitch *et al.* (2012) in WRF: Notes on using the mesoscale wind farm parameterization of Fitch *et al.* (2012) in WRF, Wind Energy, 19, 1757–1758, https://doi.org/10.1002/we.1945, 2016.

Fitch, A. C., Olson, J. B., Lundquist, J. K., Dudhia, J., Gupta, A. K., Michalakes, J., and Barstad, I.: Local and Mesoscale Impacts of Wind Farms as Parameterized in a Mesoscale NWP Model, Monthly Weather Review, 140, 3017–3038, https://doi.org/10.1175/MWR-D-11-00352.1, 2012.

Fitch, A. C., Lundquist, J. K., and Olson, J. B.: Mesoscale Influences of Wind Farms throughout a Diurnal Cycle, Monthly Weather Review, 141, 2173–2198, https://doi.org/10.1175/MWR-D-12-00185.1, 2013a.

Fitch, A. C., Olson, J. B., and Lundquist, J. K.: Parameterization of Wind Farms in Climate Models, Journal of Climate, 26, 6439–6458, https://doi.org/10.1175/JCLI-D-12-00376.1, 2013b.

Frandsen, S. T., Jørgensen, H. E., Barthelmie, R., Rathmann, O., Badger, J., Hansen, K., Ott, S., Rethore, P.-E., Larsen, S. E., and Jensen, L. E.: The making of a second-generation wind farm efficiency model complex, Wind Energy, 12, 445–458, https://doi.org/10.1002/we.351, 2009.

Hong, S.-Y., Dudhia, J., and Chen, S.-H.: A Revised Approach to Ice Microphysical Processes for the Bulk Parameterization of Clouds and Precipitation, Monthly Weather Review, 132, 103–120, https://doi.org/10.1175/1520-0493(2004)132<0103:ARATIM>2.0.CO;2, 2004.

Hunter, J. D.: Matplotlib: A 2D graphics environment, Computing in Science & Engineering, 9, 90–95, https://doi.org/10.1109/MCSE.2007.55, 2007.

Jimenez, P. A., Dudhia, J., González-Rouco, J. F., Navarro, J., Montávez, J. P., and García-Bustamante, E.: A Revised Scheme for the WRF Surface Layer Formulation, Monthly Weather Review, 140, 898–918, https://doi.org/10.1175/MWR-D-11-00056.1, 2012.

Jimenez, P. A., Navarro, J., Palomares, A. M., and Dudhia, J.: Mesoscale modeling of offshore wind turbine wakes at the wind farm resolving scale: a composite-based analysis with the Weather Research and Forecasting model over Horns Rev: Mesoscale modeling at the wind farm resolving scale, Wind Energy, 18, 559–566, https://doi.org/10.1002/we.1708, 2015.

Kain, J. S.: The Kain–Fritsch Convective Parameterization: An Update, Journal of Applied Meteorology, 43, 170–181, https://doi.org/10.1175/1520-0450(2004)043<0170:TKCPAU>2.0.CO;2, 2004.

25

30

35

Keith, D. W., DeCarolis, J. F., Denkenberger, D. C., Lenschow, D. H., Malyshev, S. L., Pacala, S., and Rasch, P. J.: The influence of large-scale wind power on global climate, Proceedings of the National Academy of Sciences, 101, 16 115–16 120, https://doi.org/10.1073/pnas.0406930101, 2004.

Lee, J. C. Y. and Lundquist, J. K.: Evaluation of the wind farm parameterization in the Weather Research and Forecasting model (version 3.8.1) with meteorological and turbine power data, Geosci. Model Dev., p. 16, https://doi.org/https://doi.org/10.5194/gmd-10-4229-2017, 2017a.

Lee, J. C. Y. and Lundquist, J. K.: Observing and Simulating Wind-Turbine Wakes During the Evening Transition, Boundary-Layer Meteorology, 164, 449–474, https://doi.org/10.1007/s10546-017-0257-y, 2017b.

Lissaman, P. B. S.: Energy Effectiveness of Arbitrary Arrays of Wind Turbines, Journal of Energy, 3, 323–328, https://doi.org/10.2514/3.62441, 1979.

Lundquist, J. K., DuVivier, K. K., Kaffine, D., and Tomaszewski, J. M.: Costs and consequences of wind turbine wake effects arising from uncoordinated wind energy development, Nature Energy, https://doi.org/10.1038/s41560-018-0281-2, 2018.

Mangara, R. J., Guo, Z., and Li, S.: Performance of the Wind Farm Parameterization Scheme Coupled with the Weather Research and Forecasting Model under Multiple Resolution Regimes for Simulating an Onshore Wind Farm, Advances in Atmospheric Sciences, 36, 119–132, https://doi.org/10.1007/s00376-018-8028-3, 2019.

Marjanovic, N., Mirocha, J. D., Kosović, B., Lundquist, J. K., and Chow, F. K.: Implementation of a generalized actuator line model for wind turbine parameterization in the Weather Research and Forecasting model, Journal of Renewable and Sustainable Energy, 9, 063 308, https://doi.org/10.1063/1.4989443, 2017.

Miller, L. M. and Keith, D. W.: Climatic Impacts of Wind Power, Joule, https://doi.org/10.1016/j.joule.2018.09.009, 2018.

Miller, L. M., Brunsell, N. A., Mechem, D. B., Gans, F., Monaghan, A. J., Vautard, R., Keith, D. W., and Kleidon, A.: Two methods for estimating limits to large-scale wind power generation, Proceedings of the National Academy of Sciences, 112, 11 169–11 174, https://doi.org/10.1073/pnas.1408251112, 2015.

Mirocha, J. D., Kosović, B., Aitken, M. L., and Lundquist, J. K.: Implementation of a generalized actuator disk wind turbine model into the weather research and forecasting model for large-eddy simulation applications, Journal of Renewable and Sustainable Energy, 6, https://doi.org/10.1063/1.4861061, 2014.

Mlawer, E. J., Taubman, S. J., Brown, P. D., Iacono, M. J., and Clough, S. A.: Radiative transfer for inhomogeneous atmospheres: RRTM, a validated correlated-k model for the longwave, Journal of Geophysical Research: Atmospheres, 102, 16 663–16 682, https://doi.org/10.1029/97JD00237, 1997.

Nakanishi, M. and Niino, H.: An Improved Mellor–Yamada Level-3 Model: Its Numerical Stability and Application to a Regional Prediction of Advection Fog, Boundary-Layer Meteorology, 119, 397–407, https://doi.org/10.1007/s10546-005-9030-8, 2006.

Nygaard, N. G.: Wakes in very large wind farms and the effect of neighbouring wind farms, Journal of Physics: Conference Series, 524, 012 162, https://doi.org/10.1088/1742-6596/524/1/012162, 2014.

Nygaard, N. G. and Hansen, S. D.: Wake effects between two neighbouring wind farms, Journal of Physics: Conference Series, 753, 032 020, https://doi.org/10.1088/1742-6596/753/3/032020, 2016.

Nygaard, N. G. and Newcombe, A. C.: Wake behind an offshore wind farm observed with dual-Doppler radars, Journal of Physics: Conference Series, 1037, 072 008, https://doi.org/10.1088/1742-6596/1037/7/072008, 2018.

Pan, Y. and Archer, C. L.: A Hybrid Wind-Farm Parametrization for Mesoscale and Climate Models, Boundary-Layer Meteorology, 168, 469–495, https://doi.org/10.1007/s10546-018-0351-9, 2018.

Platis, A., Siedersleben, S. K., Bange, J., Lampert, A., Bärfuss, K., Hankers, R., Cañadillas, B., Foreman, R., Schulz-Stellenfleth, J., Djath, B., Neumann, T., and Emeis, S.: First in situ evidence of wakes in the far field behind offshore wind farms, Scientific Reports, 8, 2163, https://doi.org/10.1038/s41598-018-20389-y, 2018.

Pryor, S. C., Barthelmie, R. J., and Shepherd, T. J.: The Influence of Real-World Wind Turbine Deployments on Local to Mesoscale Climate, Journal of Geophysical Research: Atmospheres, 123, 5804–5826, https://doi.org/10.1029/2017JD028114, 2018.

Rajewski, D. A., Takle, E. S., Lundquist, J. K., Oncley, S., Prueger, J. H., Horst, T. W., Rhodes, M. E., Pfeiffer, R., Hatfield, J. L., Spoth, K. K., and Doorenbos, R. K.: Crop Wind Energy Experiment (CWEX): Observations of Surface-Layer, Boundary Layer, and Mesoscale Interactions with a Wind Farm, Bulletin of the American Meteorological Society, 94, 655–672, https://doi.org/10.1175/BAMS-D-11-00240.1, 2013.

Rajewski, D. A., Takle, E. S., Prueger, J. H., and Doorenbos, R. K.: Toward understanding the physical link between turbines and microclimate impacts from in situ measurements in a large wind farm: Microclimate With Turbines ON Versus OFF, Journal of Geophysical Research: Atmospheres, https://doi.org/10.1002/2016JD025297, 2016.

Redfern, S., Olson, J. B., Lundquist, J. K., and Clack, C. T. M.: Incorporation of the Rotor-Equivalent Wind Speed into the Weather Research and Forecasting Model's Wind Farm Parameterization, Monthly Weather Review, 147, 1029–1046, https://doi.org/10.1175/MWR-D-18-0194.1, 2019.

Sanchez Gomez, M. and Lundquist, J. K.: The effect of wind direction shear on turbine performance in a wind farm in central Iowa, Wind Energy Science Discussions, pp. 1–23, https://doi.org/10.5194/wes-2019-22, 2019.

Sanderse, B., van der Pijl, S. P., and Koren, B.: Review of computational fluid dynamics for wind turbine wake aerodynamics, Wind Energy, 14, 799–819, https://doi.org/10.1002/we.458, 2011.

Schmitz, S.: XTurb-PSU: A Wind Turbine Design and Analysis Tool, 2012.

Siedersleben, S. K., Lundquist, J. K., Platis, A., Bange, J., Bärfuss, K., Lampert, A., Cañadillas, B., Neumann, T., and Emeis, S.: Micrometeorological impacts of offshore wind farms as seen in observations and simulations, Environmental Research Letters, 13, 124 012, https://doi.org/10.1088/1748-9326/aaea0b, 2018a.

Siedersleben, S. K., Platis, A., Lundquist, J. K., Lampert, A., Bärfuss, K., Cañadillas, B., Djath, B., Schulz-Stellenfleth, J., Bange, J., Neumann, T., and Emeis, S.: Evaluation of a Wind Farm Parametrization for Mesoscale Atmospheric Flow Models with Aircraft Measurements, Meteorologische Zeitschrift, 27, 401–415, https://doi.org/10.1127/metz/2018/0900, 2018b.

Siedersleben, S. K., Platis, A., Lundquist, J. K., Djath, B., Lampert, A., Bärfuss, K., Canadillas, B., Schultz-Stellenfleth, J., Bange, J., Neumann, T., and Emeis, S.: Observed and simulated turbulent kinetic energy (WRF 3.8.1) overlarge offshore wind farms, Geoscientific Model Development Discussions, pp. 1–29, https://doi.org/10.5194/gmd-2019-100, 2019.

Skamarock, W. C. and Klemp, J. B.: A time-split nonhydrostatic atmospheric model for weather research and forecasting applications, Journal of Computational Physics, 227, 3465–3485, https://doi.org/10.1016/j.jcp.2007.01.037, 2008.

Smith, C. M., Barthelmie, R. J., and Pryor, S. C.: *In situ* observations of the influence of a large onshore wind farm on near-surface temperature, turbulence intensity and wind speed profiles, Environmental Research Letters, 8, 034 006, https://doi.org/10.1088/1748-9326/8/3/034006, 2013.

Smith, E. N., Gebauer, J. G., Klein, P. M., Fedorovich, E., Gibbs, J. A., Smith, E. N., Gebauer, J. G., Klein, P. M., Fedorovich, E., and Gibbs, J. A.: The Great Plains Low-Level Jet during PECAN: Observed and Simulated Characteristics, Monthly Weather Review, https://doi.org/10.1175/MWR-D-18-0293.1, 2019.

Sørensen, J. N. and Shen, W. Z.: Numerical Modeling of Wind Turbine Wakes, Journal of Fluids Engineering, 124, https://doi.org/10.1115/1.1471361, 2002.

Tomaszewski, J. M., Lundquist, J. K., Churchfield, M. J., and Moriarty, P. J.: Do wind turbines pose roll hazards to light aircraft?, Wind Energy Science, 3, 833–843, https://doi.org/10.5194/wes-3-833-2018, 2018.

Troldborg, N., Sørensen, J. N., and Mikkelsen, R. F.: Numerical simulations of wake characteristics of a wind turbine in uniform inflow, Wind Energy, 13, 86–99, https://doi.org/10.1002/we.345, 2010.

Vanderwende, B. and Lundquist, J. K.: Could Crop Height Affect the Wind Resource at Agriculturally Productive Wind Farm Sites?, Boundary-Layer Meteorology, 158, 409–428, https://doi.org/10.1007/s10546-015-0102-0, 2016.

Vanderwende, B. J., Lundquist, J. K., Rhodes, M. E., Takle, E. S., and Irvin, S. L.: Observing and Simulating the Summertime Low-Level Jet in Central Iowa, Monthly Weather Review, 143, 2319–2336, https://doi.org/10.1175/MWR-D-14-00325.1, 2015.

Vanderwende, B. J., Kosović, B., Lundquist, J. K., and Mirocha, J. D.: Simulating effects of a wind-turbine array using LES and RANS: Simulating turbines using LES and RANS, Journal of Advances in Modeling Earth Systems, https://doi.org/10.1002/2016MS000652, 2016.

Vautard, R., Thais, F., Tobin, I., Bréon, F.-M., de Lavergne, J.-G. D., Colette, A., Yiou, P., and Ruti, P. M.: Regional climate model simulations indicate limited climatic impacts by operational and planned European wind farms, Nature Communications, 5, 3196, https://doi.org/10.1038/ncomms4196, 2014.

Vermeer, L., Sørensen, J., and Crespo, A.: Wind turbine wake aerodynamics, Progress in Aerospace Sciences, 39, 467–510, https://doi.org/10.1016/S0376-0421(03)00078-2, 2003.

Volker, P. J. H., Badger, J., Hahmann, A. N., and Ott, S.: The Explicit Wake Parametrisation V1.0: a wind farm parametrisation in the mesoscale model WRF, Geoscientific Model Development, 8, 3715–3731, https://doi.org/10.5194/gmd-8-3715-2015, 2015.

Wang, Q., Luo, K., Wu, C., and Fan, J.: Impact of substantial wind farms on the local and regional atmospheric boundary layer: Case study of Zhangbei wind power base in China, Energy, 183, 1136–1149, https://doi.org/10.1016/j.energy.2019.07.026, 2019.

Xia, G., Zhou, L., Minder, J. R., Fovell, R. G., and Jimenez, P. A.: Simulating impacts of real-world wind farms on land surface temperature using the WRF model: physical mechanisms, Climate Dynamics, https://doi.org/10.1007/s00382-019-04725-0, 2019.

Zhou, L., Tian, Y., Baidya Roy, S., Thorncroft, C., Bosart, L. F., and Hu, Y.: Impacts of wind farms on land surface temperature, Nature Climate Change, 2, 539–543, https://doi.org/10.1038/nclimate1505, 2012.